Predictive Modeling of Hypersonic Boundary Layer Transition with Stochastic Distributed Surface Roughness

Albert Y. Lin* and Steven A. E. Miller†

University of Florida, Gainesville, Florida, 32459, U.S.A.

A high degree of uncertainty exists in current transition prediction methods due to reliance on equivalent sand grain roughness and roughness-transition correlations derived from empirical data. Roughness effects are not properly accounted for and applicability of empirical-based correlations are limited, particularly in the hypersonic regime. This technological gap is addressed by incorporating a novel surface roughness model into CFD, which utilizes measurable statistical parameters to simulate the stochastic characteristics of realistic surfaces. Distributed roughness features are generated based on user-defined statistics and stochastic roughness effects on hypersonic transition are compared with existing roughness-transition models derived from experimental data. The effectiveness of the stochastic roughness model is assessed by comparing CFD flow-field solutions and transition onset predictions of axisymmetric cones with stochastic surface roughness versus contemporary roughness-transition correlation models. Comparisons with the Passive Nosetip Technology wind tunnel tests, ballistic range data, and Stetson sharp cone experiment are conducted to validate the methodology.

I. Nomenclature

a	=	Upper-bound of uniform distribution
a	=	Proportionality constant
AoA	=	Angle of attack
b	=	Lower-bound of uniform distribution
$\mathbb{C}_{abl}$	=	Stochastic roughness model ablation factor
$\mathbb{C}_{sign}$	=	Stochastic roughness model sign factor
d	=	Base diameter
H	=	Enthalpy
k	=	Sand grain roughness height
k_s	=	Equivalent sand grain roughness height
L	=	Axial length
n	=	Power index
$N(\mathrm{M},\sigma)$	=	Normal distribution
R_a	=	Mean roughness height
r_n	=	Nose radius
R_p	=	Roughness peak
R_q	=	RMS roughness height
R_v	=	Roughness valley depth

* Department of Mechanical and Aerospace Engineering, University of Florida, alin1@ufl.edu, albert.lin.1@us.af.mil, AIAA Student Member.
† DARPA Director's Fellow for Hypersonics and Associate Professor of Mechanical and Aerospace Engineering, Theoretical Fluid Dynamics and Turbulence Group, Department of Mechanical & Aerospace Engineering, University of Florida, 331 MAE-A, P. O. Box 116250, Gainesville, FL 32611, saem@ufl.edu; saemiller@gmail.com, AIAA Associate Fellow and lifetime member.

R_z	=	Roughness peak-to-valley
$rand$	=	Randomly-generated real number
Re_θ	=	Momentum thickness Reynolds number
s_k	=	Skewness
$[sta]$	=	Station number
$\mathbb{u}$	=	Uniformly-distributed random real number
U(a,b)	=	Uniform distribution
$\mathbb{X}_e$	=	Quantity at boundary layer edge
$\mathbb{X}_{input}$	=	Stochastic roughness model input quantity
$\mathbb{X}_k$	=	Quantity at sand grain roughness height
$\mathbb{X}_{measured}$	=	Measured quantity
$\mathbb{X}_{tr}$	=	Quantity at transition
$\mathbb{X}_w$	=	Quantity at the wall
$\mathbb{X}_\infty$	=	Freestream quantity
$[X]$	=	Disturbance parameter
$[Y]$	=	Transition parameter
z_0	=	Stochastic roughness model wall-normal data point
δ	=	Boundary layer thickness
M	=	Statistical distribution mean
σ	=	Statistical distribution standard deviation
θ	=	Momentum thickness

II. Introduction

A high degree of uncertainty exists in current transition prediction methods due to reliance on k_s and empirical correlations. Additionally, roughness effects are generally neglected during the development of high-speed vehicle aerodynamic models. Actual surface roughness always differs from the idealized geometries utilized during developmental test phases of flight vehicles. These geometries may also change unexpectedly during high-speed flight. The roughness of a vehicle's exterior paint or coating system may deviate from its design specifications, sometimes significantly, depending on the degree of thermal and shear stress experienced during flight. The outer mold line (OML) materials are most susceptible to degradation during the harsh environmental conditions of hypersonic flight, which can lead to differences between flight test telemetry data, wind tunnel tests (WTT), and computational fluid dynamics (CFD) simulations. Although designers consider these matters, it is extremely difficult to obtain quantifiable data to determine how different the actual surface geometry is versus what is being modeled due to the cost and logistics of recovering test assets.

Surface roughness has a major impact on boundary layer stability and transition, which influences heat transfer and aerodynamic performance of hypersonic flight vehicles [21]. Despite the importance of surface roughness on transition, there is a lack of understanding of how distributed surface roughness features (e.g., severity, type, and location) changes the transition process with respect to receptivity, linear stability, and nonlinear breakdown to turbulence [18]. Significant research has been conducted in recent decades to characterize surface roughness effects on transition, which has led to incorporation of roughness models into advanced CFD codes to predict hypersonic transition. However, existing roughness models rely heavily on empirical data, which restricts its applicability and can lead to inaccurate predictions [21]. Despite recent progress on understanding surface roughness effects, the major hurdles which have prevented validation of hypersonic transition prediction tools include scarcity of experimental data, limited ground test facilities, and prohibitive cost of creating flight test assets.

A. Previous Investigations and Methodology

Currently, no universal correction method can accurately predict flow over surfaces with irregular or random roughness [13]. This is an issue because stochastic roughness is present on all vehicles. Irregular surface features can originate from imperfections during production processes or be obtained from the flight environment, including effects like thermal degradation of exterior paint and coatings, rain erosion effects, or surface damage incurred during captive carriage or free-flight. Existing roughness correlations based on k_s, empirical correlations, or the e^N method have limited applicability in predicting transition on flight vehicles because surface roughness effects are not accurately represented. Classical empirical correlations that rely on Reynolds number or Mach for predicting transition also have limitations in accuracy and reliability, often displaying uncertainties exceeding a factor of three or more when compared with experimental data [6]. Furthermore, traditional techniques that rely on correlations involving only one or two parameters (from the dozens that affect transition) can only be employed in scenarios that closely resemble the conditions from which the empirical data was extracted, meaning extrapolation of empirical correlations for flight predictions involves a large degree of uncertainty [6].

Hollis [10] conducted a comprehensive study to establish roughness-transition correlations based on experimental flight test, wind tunnel, and ballistic range data collected over 50 years. These roughness-transition correlations are power law relationships between a transition parameter and disturbance parameter:

$$[Y]_{tr} = a[X]^n \tag{1}$$

where the proportionality constant and power index are derived from regression analyses of empirical data [10]. Reda first introduced the power-law relationship (Figure 1, top left) as a framework to describe roughness-induced transition for ballistic range experiments [19]. The most widely accepted roughness-transition correlations were derived from the Passive Nosetip Technology (PANT) wind tunnel tests (WTT) [1,3,11,12] and ballistic range tests conducted by Reda [7,8,9,10] to model the effects of distributed surface roughness on boundary layer transition [2].

The PANT correlation (2) is accepted as the standard for correlating wind tunnel transition data with distributed roughness, whereas the Reda Correlation (3) is widely accepted as the standard for correlating roughness data obtained from ballistic range tests [10]. Extensive experimental data supports using the PANT and Reda correlations to model roughness effects in CFD for wind tunnel and ballistic range data, respectively. However, these correlations are not interchangeable. To address these differences, a combined correlation (4) was developed which fits wind tunnel, ballistic range, and flight test data. Figure 1 also shows how these correlations compare with experimental data.

$$[Re_\theta]_{tr} = 215\left[\left(\frac{k}{\theta}\right)\left(\frac{T_e}{T_w}\right)\right]^{-0.7} \tag{2}$$

$$[Re_\theta]_{tr} = 250\left[\left(\frac{\rho_k u_k}{\rho_e u_e}\right)\left(\frac{k}{\theta}\right)\left(\frac{\mu_e}{\mu_w}\right)\right]^{-1} \tag{3}$$

$$[Re_\theta]_{tr} = 165\left[\left(\frac{k}{\theta}\right)\left(\frac{T_e}{T_w}\right)\left(\frac{H_e}{H_w}\right)^{-1} M_e^{\ (-0.5)}\right]^{-0.5} \tag{4}$$

The quantity $\mathbb{X}_{tr}$ defines the parameter at transition, k/θ is the roughness height to momentum thickness ratio, T_e/T_w is the boundary layer edge temperature to wall temperature ratio, ρ_k/ρ_e is the sand grain roughness height density to boundary layer edge density ratio, u_k/u_e is the sand grain roughness height velocity to boundary layer edge velocity ratio, μ_k/μ_e is the sand grain roughness height dynamic viscosity to boundary layer edge dynamic viscosity ratio, and H_e/H_w is the boundary layer edge enthalpy to wall enthalpy ratio. Power-law relationships were also derived for transition limits of vehicles with smooth and ultra-smooth walls. Equations (5) and (6) are "rule-of-thumb" guidelines often used by designers for predicting transition on smooth-walled vehicles [2]:

$$[Re_\theta]_{tr} = 250 \pm 100 \quad \left\{ 0.01 < \frac{k}{\delta} < 0.1 \quad \text{(smooth wall limit)} \right. \tag{5}$$

$$[Re_\theta]_{tr} = 500 \pm 200 \quad \left\{ \frac{k}{\delta} < 0.01 \quad \text{(ultrasmooth wall limit)} \right. \tag{6}$$

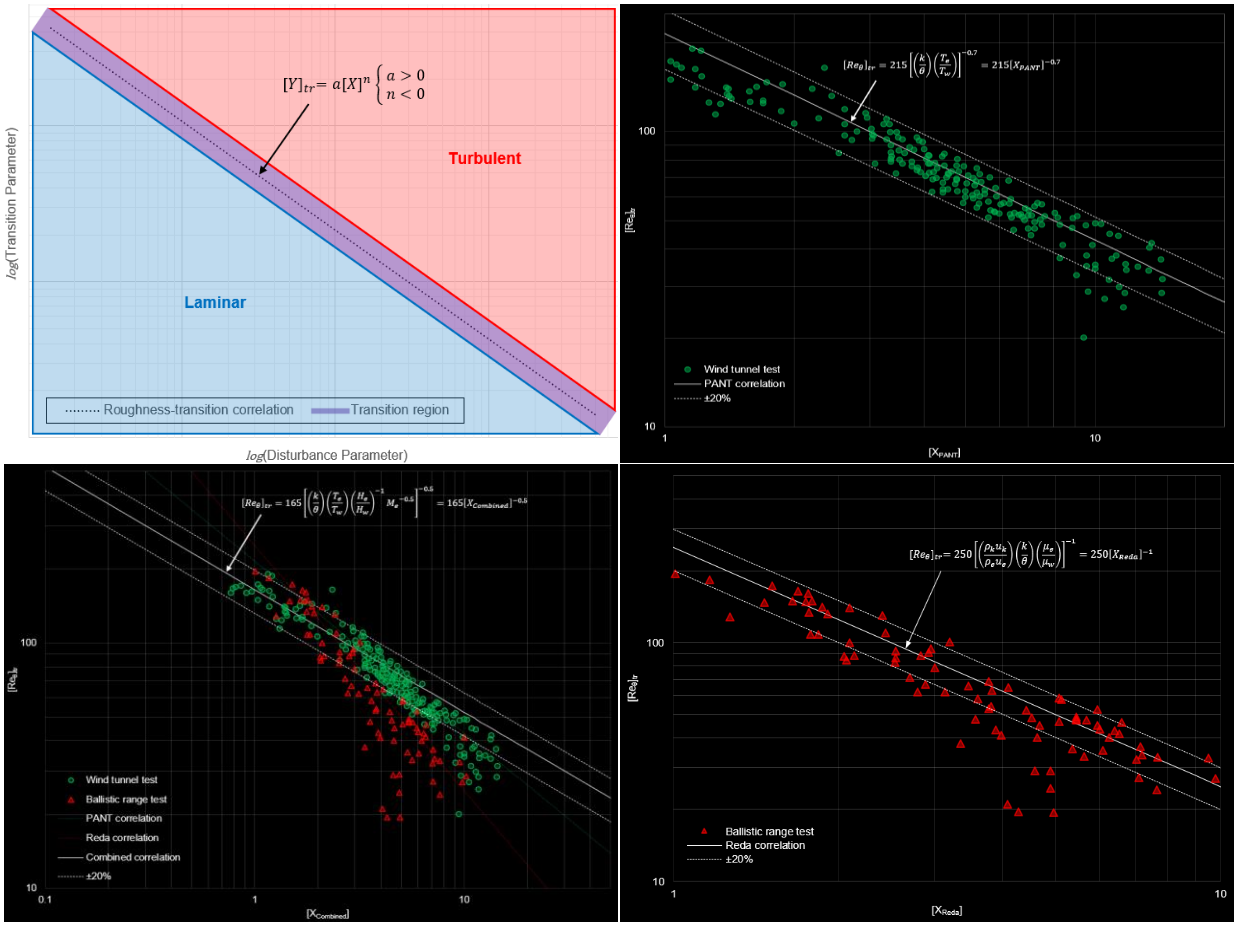

Fig. 1. Roughness-transition power law relationship between $[Y]_{tr}$ and $[X]$ (top left) and PANT, Reda, and combined correlations compared with experimental data (top right, bottom right, bottom left).

III. Methodology

A. Present Approach

Current simulation methodologies utilizing uniform surface profiles to represent the effect of roughness can be unreliable for predicting transition. To address this deficiency, a computationally efficient method was developed to generates OMLs with stochastic roughness, using statistical surface roughness measurements as inputs. The research methodology is outlined in Figure 2. The stochastic roughness model was developed in Fortran and integrated into the Langley Aerothermodynamic Upwind Relaxation Algorithm (LAURA) v5.6 source code [15]. It leverages standard surface roughness measurements, such as ones obtained using precision surface measurement equipment, to simulate realistic surface irregularities (such as orange-peel roughness). Stochastic surface roughness is modeled using normally distributed random values using the Box-Muller method.

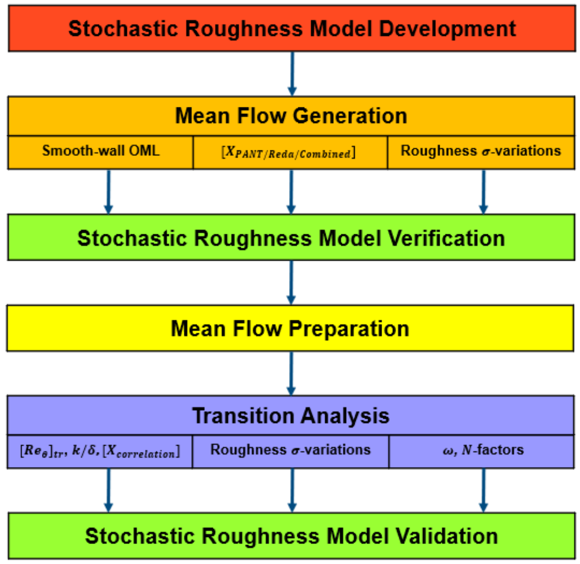

Fig. 2. Methodology for stochastic roughness model development, verification, and validation.

B. Stochastic Roughness Model Development

The stochastic roughness model was developed using user-defined statistical roughness parameters to define OML roughness features. Figure 3 illustrates these roughness parameters and emphasizes the random nature of realistic surface roughness. These parameters were selected for their accessibility, as they can be readily obtained using standard surface roughness measurement tools (Table 1). Roughness is not applied to the nosecap region but begins on the cone section immediately afterward, as this area is more susceptible to material degradation.

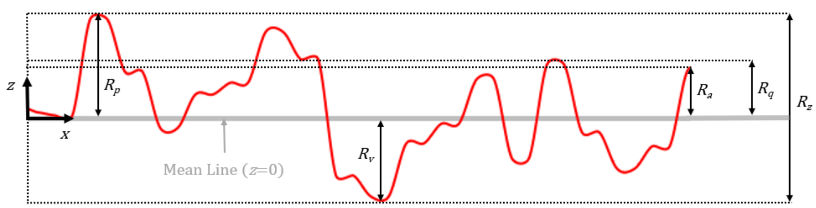

Fig. 3. Example of a surface roughness measurement exhibiting the stochastic nature of surface roughness features.

Table 1. Definition of roughness parameters.

Parameter	Description	Discrete Implementation
R_a	Mean roughness height	$\frac{1}{n}\sum_{i=1}^{n}\lvert z_i\rvert$
R_q	RMS roughness	$\sqrt{\frac{1}{n}\sum_{i=1}^{n} z_i^2}$
R_p	Maximum peak height above mean line	$\max(z_i)$
R_v	Maximum valley depth below mean line	$\min(z_i)$
R_z	Maximum peak-to-valley height	$R_p + \lvert R_v\rvert$
s_k	Skewness	$\frac{1}{n(R_q)^3}\sum_{i=1}^{n} z_i^3$

The stochastic roughness model shape function is defined as:

$$z(R_a, R_q) = \mathbb{C}_{sign}(1 - \mathbb{C}_{abl})(\sigma * z_0) \tag{7}$$

where

$$z_0 = \begin{cases} 1.1R_a(rand_1), \text{if using } R_a \\ R_q(rand_2), \text{if using } R_q \end{cases} \tag{8}$$

$$rand_1 \sim N(0,1) \tag{9}$$

$$rand_2 \sim N(0,1) \tag{10}$$

$$rand_3 \sim U(-1,1) \tag{11}$$

$$\mathbb{C}_{sign} = \begin{cases} 1 \text{ if } rand_3 > 0 \\ -1 \text{ if } rand_3 < 0 \end{cases} \tag{12}$$

σ is the standard deviation and $\mathbb{C}_{abl}$ is an ablation factor which sets the bounds of R_z. $\mathbb{C}_{abl}$ is based on the ratio of R_q to R_z and can be tuned based on knowledge of material ablation characteristics. z_0 is the wall-normal data point generated by the stochastic roughness model along the axial direction. R_q (or R_a), σ, and $\mathbb{C}_{abl}$ are the only user inputs required for the stochastic roughness model. This is by design to keep model inputs simplistic and enable use of statistical data from common surface roughness measurement tools such as stylus profilometers or non-contact optical systems. The scope of this research considers only symmetric roughness profiles, characterized by an equal distribution of peaks and valleys. Therefore, the model does not include skewness or kurtosis as inputs to alter the symmetry of the roughness profile.

Randomly-generated real numbers are denoted by $rand_1$, $rand_2$, and $rand_3$. $rand_1$ and $rand_2$ are generated based on a normal distribution, represented by $N(\mathrm{M}, \sigma)$, where M is the mean and σ is the standard deviation. The purpose of $rand_1$ and $rand_2$ are to generate random, normally distributed scaling factors between 0 and 1. These values are applied to the input roughness statistics (R_a or R_q) to generate the OML. The stochastic roughness model is designed to represent R_q. Therefore, if R_a is used as the model input, then z_0 is calculated using the measurement rule-of-thumb of $R_q \sim 1.1R_a$. $rand_3$ is generated based on a uniform distribution, represented by U(a,b), where a and b are the upper and lower bounds of the distribution, respectively. $\mathbb{C}_{sign}$ applies a random, uniformly distributed sign factor based on $rand_3$ to ensure roughness points are generated above and below the OML.

C. CFD Configuration

LAURA is a contemporary CFD code developed by NASA Langley which simulates high-energy, reacting flows by solving the Navier-Stokes equations using a structured, cell-centered gid system [5,26]. It has been used in simulating aerothermal environments for vehicles designed for entry, descent, and landing applications [25]. The stochastic roughness model is integrated in the source code, which is developed in Fortran 90. Fortran does not include a function to directly generate normally distributed random numbers; its random number function is only capable of generating uniformly distributed random numbers. To alleviate this issue, the Box-Muller method is implemented to convert two independent, uniformly distributed random values into two independent, normally distributed random values. Equations 13 and 14 show how $rand_1$ and $rand_2$ are calculated using the Box-Muller method to generate normally distributed random values, using uniformly distributed random values ($\mathbb{u}1$ and $\mathbb{u}2$):

$$rand_{1\_F90} = \sqrt{-2\ln(\mathbb{u}1)} * \cos(2\pi * \mathbb{u}2) \tag{13}$$

$$rand_{2\_F90} = \sqrt{-2\ln(\mathbb{u}1)} * \sin(2\pi * \mathbb{u}2) \tag{14}$$

Mean flow solutions were generated using an 11-species gas model, representing a mixture of thermally perfect gases with 76.7% nitrogen gas (N_2) and 22.3% oxygen gas (O_2). The remaining 1% consists of atomic nitrogen (N), atomic oxygen (O), nitric oxide (NO), ionized oxygen molecules (O_2^+), ionized oxygen atoms (O^+), ionized nitric oxide (NO^+), and electrons (e^-). Boundary conditions include an adiabatic wall for surface temperatures and a noncatalytic model for the solid surface. LAURA outputs aerodynamic, flow-field, and boundary layer solutions, as well as grid geometry and convergence data, which eases integration with instability solvers.

Computational grids for all cases consist of 256 axial-direction cells, one azimuthal direction cell, and 256 wall-normal cells. A subset of axial-direction cells is allocated to the nosecap region, with the number of cells varying for each test case. Sharp cones require fewer nosecap cells, while blunt cones require more to accurately resolve a larger radius of curvature. The initial grid is set to begin with 64 wall-normal direction cells and doubles in this direction each time the Euclidean norm drops below 1.0×10^{-3}, to a maximum of 256 wall-normal cells.

Grid adaptation features are active and uses a linear interpolation routine for shock alignment at a specified number of time steps and for a specified number of realignments. This parameter varies for each test case and is dependent on the geometry, flow conditions, and amount of roughness generated by the stochastic model. Grid adaptation was observed to be more sensitive as the amount of roughness was increased. Grid cells were susceptible to negative volume cells during shock alignments at large roughness values ($R_z > 10000\ \mu in$), which would crash the simulation. This is depicted in Figure 4, which shows a reduction in the far-field boundary cells as more grid alignments are conducted. As a result, the PANT-J 2σ roughness dimensions were determined to be the limit of roughness vales which could generate valid computational grids using the stochastic model.

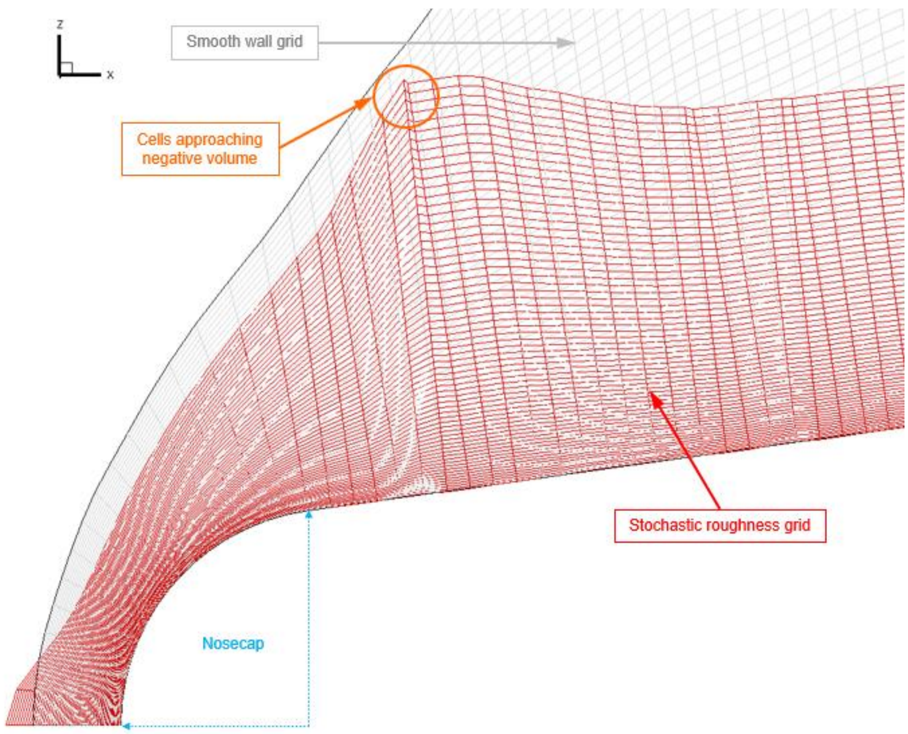

Fig. 4. Computational grid highlighting the nosecap and cells approaching negative volume.

D. Test Geometries

Generic geometries are beneficial in isolating effects on transition, instability ranges, and sensitivity levels to different flow parameters [17]. Thus, geometries and flow conditions from the PANT-J WTT [12], VKF Range G ballistic range experiment [20], and Stetson WTT [22] were selected for this research. CFD test geometries are shown in Table 2. Values for half-angle, length, and diameter of the VKF Range G tests were not explicitly disclosed in literature. However, the objective of these hyperballistic experiments was to evaluate the validity of extrapolating the PANT correlation for re-entry vehicle materials and environments [20]. Therefore, VKF Range G model geometries are assumed to be the same as PANT-J, except for the nose radius, which was specified. The focus of the Stetson WTT was not roughness-based and subsequently did not specify surface finishes on wind tunnel models. High-fidelity wind tunnel tests typically require models to be aerodynamically smooth, with surface roughness measurements of approximately 0.1 μm (3.9 μin) or better [7]. Therefore, a surface roughness of 5 μin is assumed for models from these experiments. R_a values will be adjusted to conduct a parametric study on boundary layer sensitivity to roughness height.

Table 2. CFD test cases.

Test Case	θ (°)	L (in)	d (in)	r_n (in)	R_q (μin)
PANT-J	8.0	40.0	4.224	1.5000	3500
VKF Range G	8.0	40.0	4.224	0.4300	450
Stetson	7.0	40.0	9.823	0.0015	5

E. Test Matrix

The CFD test conditions are listed in Table 3. LAURA includes options to specify the onset of transition by physical distance, Re_θ, or using a distributed roughness-transition correlation [24]. Three roughness-transition correlations are available and based on a user-defined roughness height. These correlations are based on the PANT wind tunnel tests, ballistic range data, or a hybrid correlation based on a combination of flight test, wind tunnel, and ballistic range data. LAURA requires a turbulence model to exercise these roughness-transition algorithms, so the Cebeci-Smith algebraic model was used in these cases. Table 4 lists the input parameters for the various roughness models analyzed. LAURA correlations (PANT, Reda, and combined) use roughness height as the input value, while the stochastic roughness model uses statistical roughness parameters.

Roughness measurements from the PANT-J, Stetson, and VKF Range G experiments are used for roughness height inputs. Specifics of test article geometries, flow conditions, and transition correlation data for the PANT wind tunnel and Reda ballistic range experiments are tabulated in the Hollis appendices [10]. The Stetson experiment did not specify a surface finish on the wind tunnel models. These were not roughness tests and high-performance wind tunnel experiments typically require models be aerodynamically smooth, approximately 0.1 μm (3.9 μin) or better [23]. Therefore, a roughness of 5 μin was assumed for this test case.

Table 3. CFD test conditions.

Test Case	M_∞	$Re_\infty (/m)$	$u_\infty (m/s)$	$\rho_\infty (kg/m^3)$	$T_\infty (K)$	AoA (°)
PANT-J	4.98	7.38×10^6	1109	0.0552	124	0
VKF Range G	13.09	1.72×10^7	4499	0.3157	294	0
Stetson	7.97	4.27×10^6	1186	0.0141	55	0

Table 4. CFD roughness-transition model input parameters.

Test Case	Roughness Model	R_a (μin)	R_q (μin)	σ	$\mathbb{C}_{abl}$	k (μin)
PANT-J	None	--	--	--	--	--
PANT-J	PANT	--	--	--	--	908
PANT-J	PANT	--	--	--	--	3500
PANT-J	Combined	--	--	--	--	3500
PANT-J	Stochastic	0	3500	0.5,1,1.5,2	0.28	--
VKF Range G	None	--	--	--	--	--
VKF Range G	Reda	--	--	--	--	450
VKF Range G	Combined	--	--	--	--	450
VKF Range G	Stochastic	0	450	1,2,3,6	0	--
VKF Range G	Stochastic	0	450	1	0.28	--
Stetson	None	--	--	--	--	--
Stetson	PANT	--	--	--	--	5
Stetson	Combined	--	--	--	--	5
Stetson	Stochastic	0	5	1,2,3,6	0	--

Figure 5 (left) shows the range of freestream Mach numbers, M_∞, versus $[Re_\theta]_{tr}$ for experimental roughness-transition data described by Hollis [10], along with PANT-J, VKF Range G, and Stetson CFD conditions. Roughness measurements from these tests are also provided in Figure 5 (right). These plots highlight the test conditions, showing a direct assessment of the stochastic roughness model's capability to capture transition trends across various Mach regimes and roughness heights.

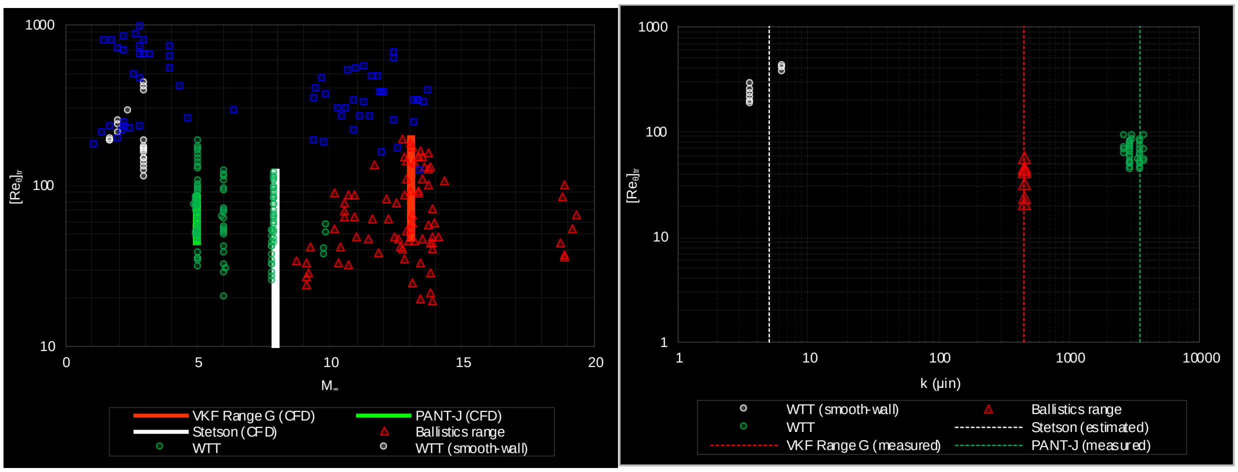

Fig. 5. M_∞ **versus** $[Re_\theta]_{tr}$ **for flight test, wind tunnel, and ballistic range experiments (left) and modeled roughness compared with wind tunnel and ballistics range roughness measurements (right).**

IV. Results

A. Stochastic Roughness Model

To verify the implementation of the stochastic roughness model in the LAURA source code, several metrics were evaluated to ensure the model generates the intended roughness features and statistics. First, roughness statistics were examined across all runs. Table 5 lists these outputs, such as the roughness input, roughness arithmetic mean, RMS roughness height, and standard deviation.

Table 5. Stochastic roughness model outputs.

Test Case	k_{input} (μin)	R_a (μin)	R_q (μin)	σ (μin)	R_p (μin)	R_v (μin)	R_z (μin)	s_k (μin)
PANT-J (0.5σ)	3500	947	1225	1176	3425	-2803	6228	0.53
PANT-J (1σ)	3500	1950	2450	2478	6944	-4919	11863	0.42
PANT-J (1.5σ)	3500	3205	3917	3796	10215	-10608	20823	-0.13
PANT-J (2σ)	3500	3795	4736	4595	12815	-14732	27547	-0.25
VKF (1σ)	450	384	435	446	1241	-1088	2329	0.06
VKF (2σ)	450	717	930	949	2233	-2285	4518	0.01
VKF (3σ)	450	1033	1456	1385	3208	-4513	7722	-0.54
VKF (6σ)	450	2188	2800	2851	7968	-6296	14265	0.26
Stetson (1σ)	5	4	5	5	13	-14	27	-0.12
Stetson (2σ)	5	8	11	11	28	-30	58	-0.08
Stetson (3σ)	5	12	16	15	30	-56	86	-0.60
Stetson (6σ)	5	23	32	30	78	-99	177	0.32

Next, variations in θ of the stochastic roughness profiles were examined. Figure 6 (left) shows θ decreasing along x/L from approximately 90° near the nosetip to a constant value for the smooth-wall OML. The stochastic roughness profile exhibits slight oscillations in θ and are observed on the stochastic roughness profile. This confirms the model is generating random points around the mean line as intended. Figure 6 (right) shows the distribution of stochastic roughness heights along the cone, RMS roughness value, and smooth-wall OML for reference and confirms roughness is applied only on the cone section, excluding the nosecap region. Finally, Figure 7 compares the modeled stochastic roughness geometry with a smooth wall, verifying the model's implementation and its ability to generate intended roughness features based on user-defined parameters.

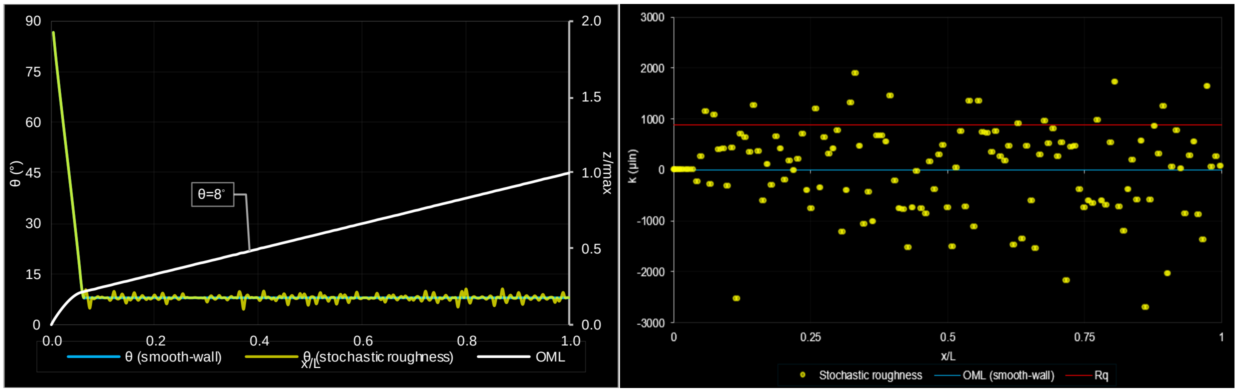

Fig. 6. Variations in θ along x/L of stochastic roughness OML, compared with constant θ of smooth-wall OML (left) and example distribution of stochastic roughness modeled along x/L (right).

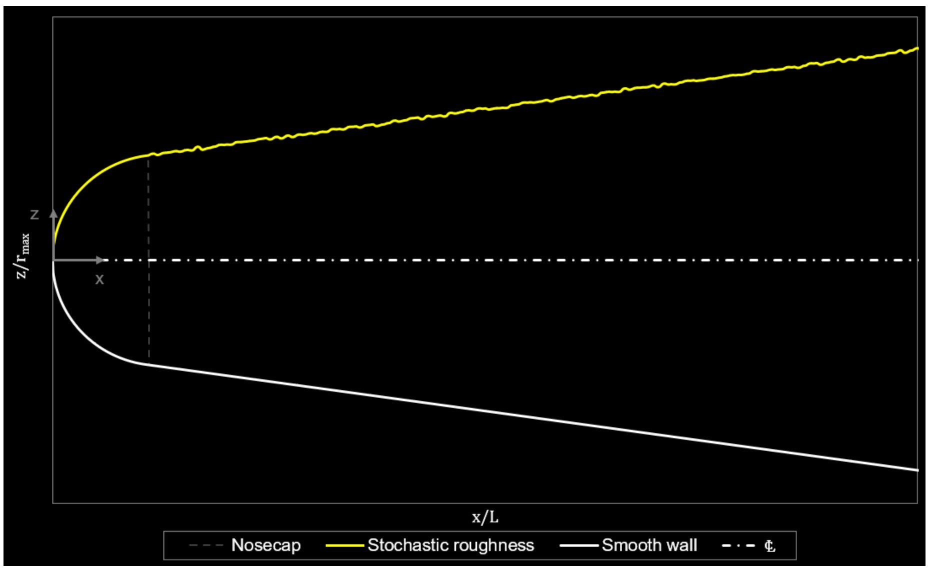

Fig. 7. Axisymmetric cone OML modeled with stochastic roughness (upper surface surface) compared with a smooth wall (lower surface).

B. CFD Results

LAURA flow-field solutions were generated for the PANT-J, VKF Range G, and Stetson test cases. Figure 8 contains all experimental wind tunnel, ballistic range, and flight test data described by Hollis [10], overlaid with baseline CFD results. The baseline CFD configuration sets k equal to the measured roughness from each respective experiment and uses the LAURA roughness-transition correlation consistent with the type of experiment (Table 6). Roughness for the Stetson test was assumed to be k = 5 μin the combined correlation was most appropriate to model this test case. Smooth and ultrasmooth-wall transition limits are shown and serves as a guideline for predicted transition regions of rough-wall surfaces from wind tunnel and ballistic range tests.

Alignment of the baseline CFD results with experimental data instills a high degree of confidence in the boundary conditions and resulting solutions (Figure 8). The Stetson CFD solution is shown but was not part of the historical roughness-transition data sources described by Hollis [10]. The small k/δ values were expected; however, the data did not align with flight test data nor other smooth-wall wind tunnel data. It should be noted that both the PANT and Stetson wind tunnel experiments were conducted in environments with inherent noise, which should be considered when interpreting these results. Ballistic range experiments provided the most applicable data with respect to a low-noise, free-flight environment and the Hollis appendices [10] contain all ballistic range test parameters.

Table 6. Baseline CFD configurations.

Test Case	Experiment	LAURA correlation	$R_{q,measured}$ (μin)	$R_{z,measured}$ (μin)	k (μin)
PANT-J	WTT	PANT	908	3500	3500
VKF Range G	Ballistic range	Reda	450	--	450
Stetson	WTT	Combined	--	--	5

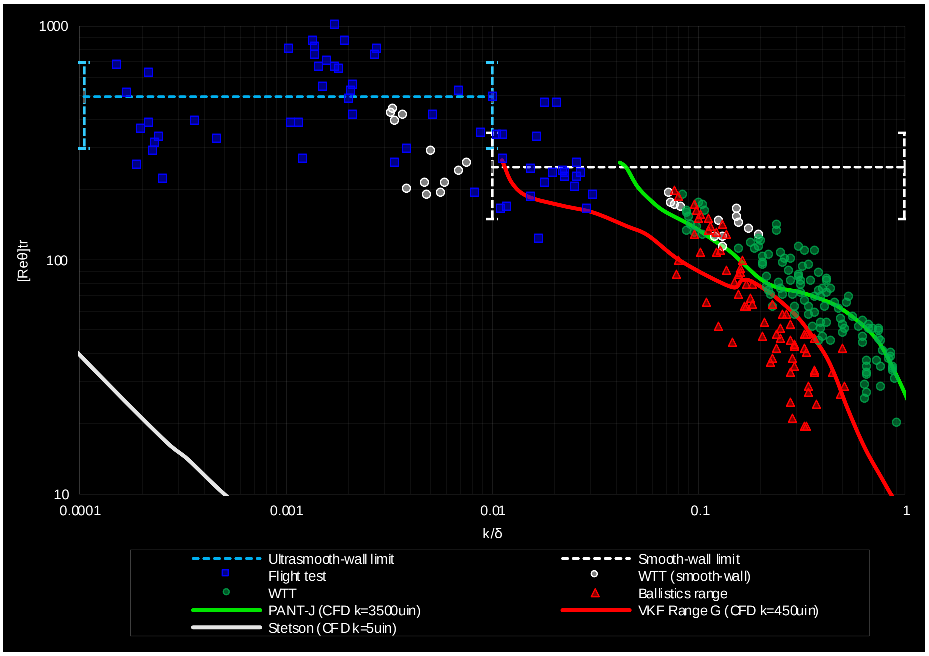

Fig. 8. $[Re_\theta]_{tr}$ versus k/δ of experimental WTT, ballistic range, and flight test data, compared with baseline CFD results.

1. PANT-J

The PANT-J test case allocated 16 axial-direction cells for the nosecap. An ablation factor of $\mathbb{C}_{abl} = 0.28$ was applied to represent the R_q/R_z ratio and baseline roughness was set as $k_{PANT-J} = 3500\ \mu in$, as specified in the test documentation [12]. Stochastic roughness levels were modeled at 0.5, 1, 1.5, and 2 standard deviations from k_{PANTJ}. The modeled RMS roughness values for these cases are plotted against $[Re_\theta]_{tr}$ in Figure 9 (left), along with wind tunnel data with comparable roughness values to illustrate the stochastic roughness levels of the PANT-J test cases.

The lower limit of smooth-wall transition is indicated at $Re_\theta \sim 150$ and rough-wall transition is expected when $k/\delta > 0.1$ and $Re_\theta < 150$. As roughness increases, the data aligns more closely with experimental data points. However, a different trend in k/δ was observed beyond one standard deviation of k. At lower roughness levels, δ and θ increased gradually along the surface. At higher roughness levels, δ and θ increased rapidly near the leading edge and indicates an earlier transition to turbulence (Figure 9, right). The rapid growth of δ affects the k/δ ratio and compromises its effectiveness as a predictor for transition regions, highlighted by the 1.5σ and 2σ roughness cases (Figure 9, right). This suggests that there is a roughness threshold beyond which the k/δ ratio loses its effectiveness in defining smooth and rough-wall boundaries.

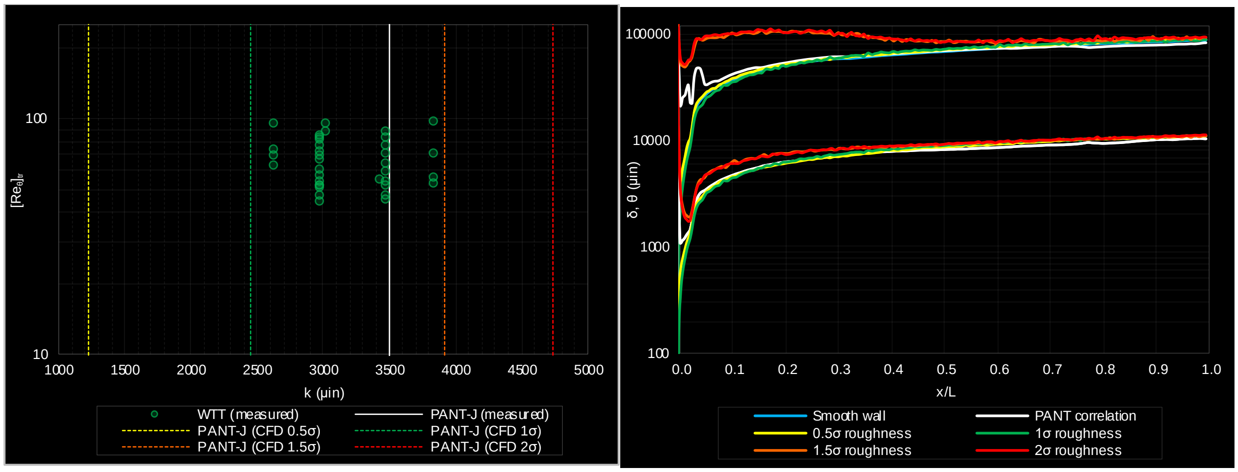

Fig. 9. PANT-J modeled roughness compared with WTT roughness measurements (left) and comparison of δ (top) and θ (bottom) along x/L of increasing roughness for $k = 3500\ \mu in$ (right).

Figure 10 (top left) shows $[Re_\theta]_{tr}$ as a function of k/δ for CFD runs with increasing stochastic roughness alongside wind tunnel data. The CFD roughness was set to $k = 3500\ \mu in$, as this value provided the best alignment with test data using the existing LAURA roughness models. By maintaining consistency in the roughness inputs, the effects of stochastic roughness can be isolated and compared with those of existing roughness-transition correlations. The most direct comparison was between the 1σ stochastic roughness model (with $R_q = 3500\ \mu in$) and PANT correlation (with $k = 3500\ \mu in$). These solutions share a similar trend. However, the 1σ stochastic roughness $[Re_\theta]_{tr}$ was biased lower by approximately 30%.

Predicted transition locations were determined by calculating the disturbance parameter, $[X_{PANT}]$, where rough-wall transition is expected. For PANT-J, the transition region was defined by $Re_\theta \sim 150$ and $0.1 < k/\delta < 1$. Figure 10 (top right) shows $[Re_\theta]_{tr}$ as a function of $[X_{PANT}]$ and compares the CFD results with experimental data and the PANT correlation. Once $[X_{PANT}]$ was determined, the transition location was mapped to an axial position. Transition metrics for the PANT-J tests cases are listed in Table 7 and Figure 10 (bottom left) illustrates an upstream shift in transition locations as stochastic roughness levels increase.

Figure 10 (bottom right) plots C_D as a function of R_q for different roughness levels, showing that drag increases with higher roughness. This trend aligns with the expectation that increased roughness promotes earlier transition to turbulence, confirming that the stochastic roughness model effectively captures roughness effects on the boundary layer. Notably, C_D was 3% higher for the 1σ stochastic roughness case compared to the PANT correlation solution, highlighting a discrepancy in drag predictions when using existing roughness-transition correlations.

Table 7. Predicted transition metrics (PANT-J, $k = 3500\ \mu in$).

Test Case	$[Re_\theta]_{tr}$	k/δ range	$[X_{correlation}]$	x/L	$[sta]_{tr}$
PANT-J (smooth wall)	150	0.1-1.0	0.00014	0.140	43
PANT-J (0.5σ)	150	0.1-1.0	0.17000	0.120	38
PANT-J (1σ)	150	0.1-1.0	0.54000	0.055	22
PANT-J (PANT correlation)	150	0.1-1.0	0.70000	0.043	19
PANT-J (1.5σ)	150	0.1-1.0	1.10000	0.031	16
PANT-J (2σ)	150	0.1-1.0	1.35000	0.031	16

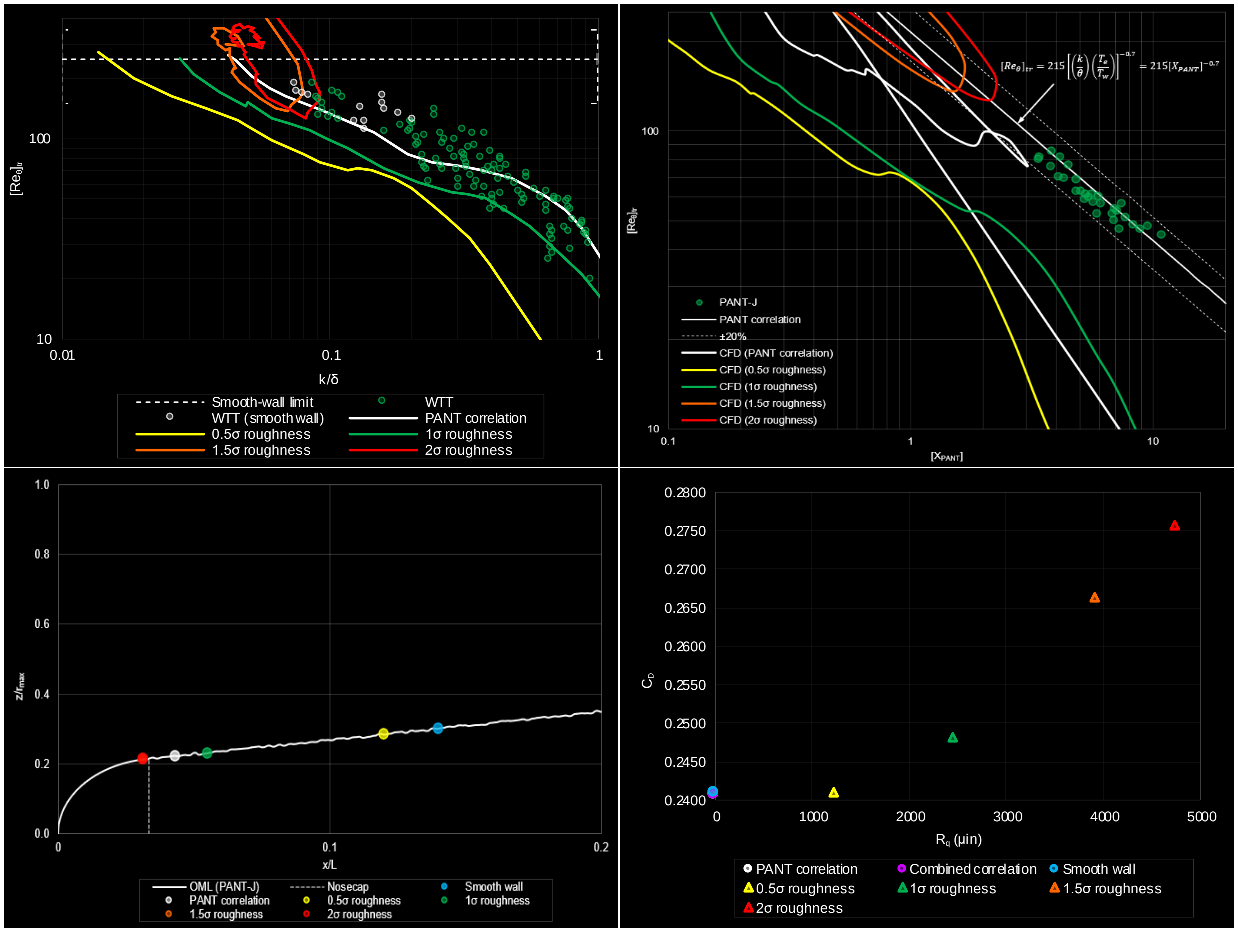

Fig. 10. PANT-J transition analyses comparing $[Re_\theta]_{tr}$ versus k/δ and $[X_{PANT}]$ (top left and right) and effect of increasing roughness on transition location and C_D (bottom left and right).

2. VKF Range G

The VKF Range G test case allocated 16 axial-direction cells for the nosecap. Baseline roughness was set as $k_{VKF} = 450\ \mu in$, as specified in the test documentation [10]. However, no ablation factor ($\mathbb{C}_{abl} = 0$) was applied to represent the R_q/R_z ratio as this was not specified in the literature. Stochastic roughness levels were modeled at 1, 2, 3, and 6 standard deviations from k_{VKF}. The modeled RMS roughness values of these cases are plotted against $[Re_\theta]_{tr}$ in Figure 11 (left), along with ballistic range data with comparable roughness values to illustrate the stochastic roughness levels of the VKF Range G test cases. Figure 11 (right) shows minimal deviations in δ and θ, with an expected increase in thickness as roughness levels rise. This indicates the stochastic roughness model is functioning as intended. Boundary layer modeling appears more stable and suggests the k/δ ratio can effectively differentiate between smooth and rough-wall boundaries for the roughness levels modeled in the VKF Range G test cases.

Figure 12 (top left) shows $[Re_\theta]_{tr}$ as a function of k/δ for CFD runs with increasing stochastic roughness alongside wind tunnel data. The CFD roughness was set to $k = 450\ \mu in$ based on test documentation and the baseline solution using the Reda correlation showed good alignment with experimental ballistic range data. The most direct comparison was between the 1σ stochastic roughness model (with $R_q = 450\ \mu in$) and Reda correlation (with $k = 450\ \mu in$), where minimal discrepancies were observed. As the roughness standard deviation was increased, the solution shifted along the k/δ axis as expected, illustrating the responsiveness of the stochastic roughness model to changes in roughness intensity. Additionally, when an ablation factor of $\mathbb{C}_{abl} = 0.28$ was applied, the CFD solution displayed better alignment with experimental data points.

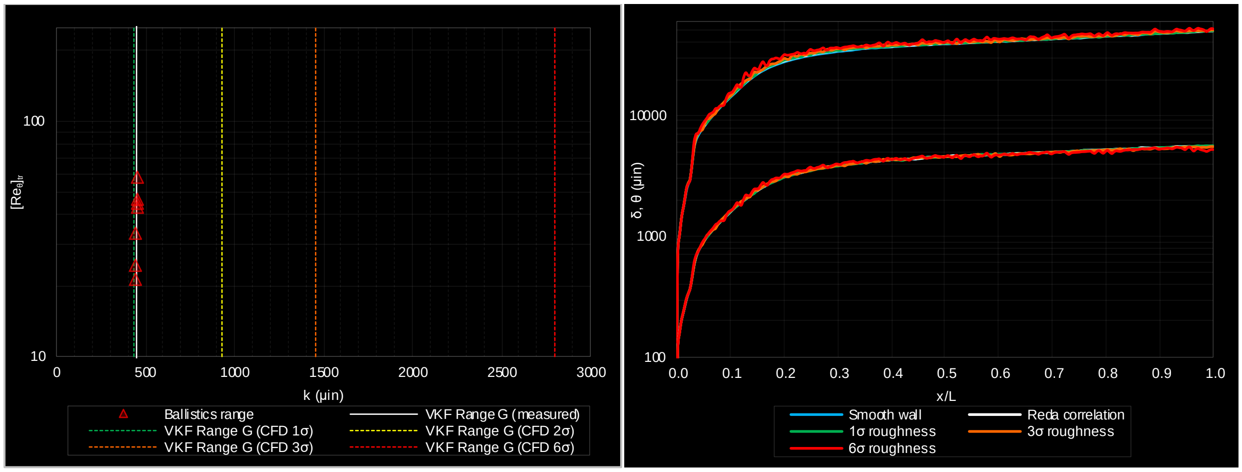

Fig. 11. VKF Range G modeled roughness compared with ballistic range roughness measurements (left) and comparison of δ (top) and θ (bottom) along x/L of increasing roughness for $k = 450\ \mu in$ (right).

The transition region was defined by $Re_\theta \sim 150$ and $0.1 < k/\delta < 1$ and Figure 12 (top right) shows $[Re_\theta]_{tr}$ as a function of $[X_{Reda}]$, comparing CFD results with experimental data and the Reda correlation. While there was good alignment between $[Re_\theta]_{tr}$ and k/δ, $[X_{Reda}]$ values initially showed less agreement with test data until roughness levels were increased. Even with higher roughness, achieving alignment with test data required a 6σ roughness level and the slope remained noticeably different from the Reda correlation. This discrepancy suggests that better agreement could be achieved by adjusting the Reda correlation constants and raises the possibility that the Reda disturbance parameters may not accurately represent ballistic range data. VKF Range G transition metrics are listed in Table 8 and Figure 12 (bottom left) shows an upstream shift in transition locations as stochastic roughness levels increased. C_D versus R_q at different roughness levels shows drag increasing with higher roughness, confirming the stochastic roughness model effectively captures roughness effects on the boundary layer (Figure 12, bottom right). Drag predictions showed minimal discrepancy between the 1σ stochastic roughness case and Reda correlation solution, with a difference in C_D of only 0.005%.

Table 8. Predicted transition metrics (VKF Range G, $k = 450\ \mu in$).

Test Case	$[Re_\theta]_{tr}$	$[X_{correlation}]$	x/L	$[sta]_{tr}$
VKF Range G (smooth wall)	150	0.00005	0.036	32
VKF Range G (1σ)	150	0.02500	0.028	29
VKF Range G (2σ)	150	0.06000	0.020	24
VKF Range G (3σ)	150	0.10000	0.017	22
VKF Range G (6σ)	150	0.20000	0.017	22

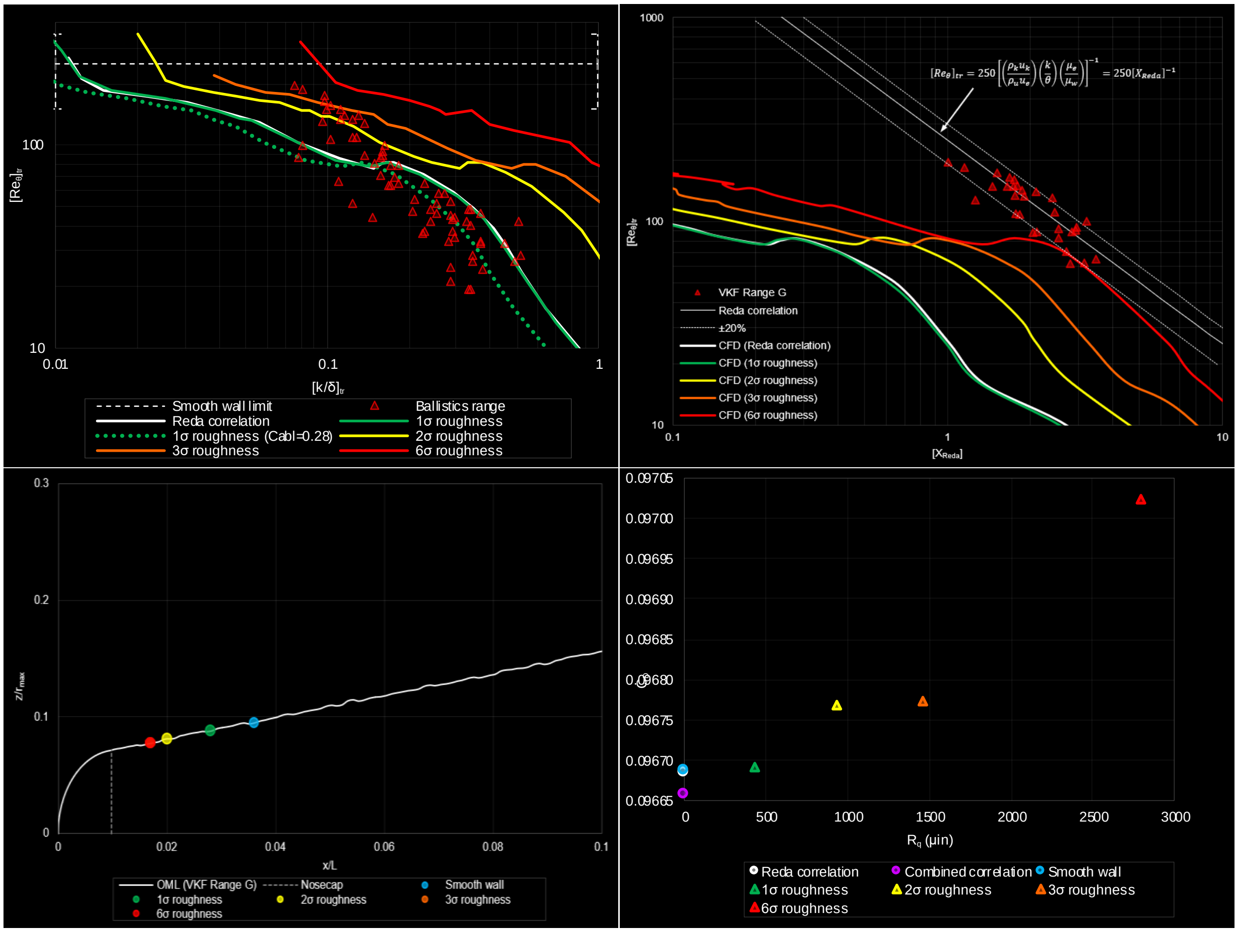

Fig. 12. VKF Range G transition analyses comparing $[Re_\theta]_{tr}$ versus k/δ and $[X_{PANT}]$ (top left and right) and effect of increasing roughness on transition location and C_D (bottom left and right).

3. *Stetson*

The Stetson test case allocated 8 axial-direction cells for the nosecap because of its sharp nose radius. Baseline roughness was set as $k_{Stetson} = 5\,\mu in$ and no ablation factor ($\mathbb{C}_{abl} = 0$) was applied to represent the R_q/R_z ratio. Stochastic roughness levels were modeled at 1, 2, 3, and 6 standard deviations from $k_{Stetson}$. The modeled RMS roughness values from these cases are plotted against $[Re_\theta]_{tr}$ in Figure 13 (left). No Stetson experimental test data was available, so smooth-wall wind tunnel data from the PANT Program with comparable roughness values were plotted to illustrate the stochastic roughness levels of the Stetson test cases. Minimal differences in δ and θ were observed across the various roughness levels due to the limited roughness modeled in the Stetson test cases (Figure 13, right). Boundary layer modeling appears stable, indicating that the k/δ ratio can effectively distinguish between smooth and rough-wall boundaries for the roughness levels applied in the Stetson test cases.

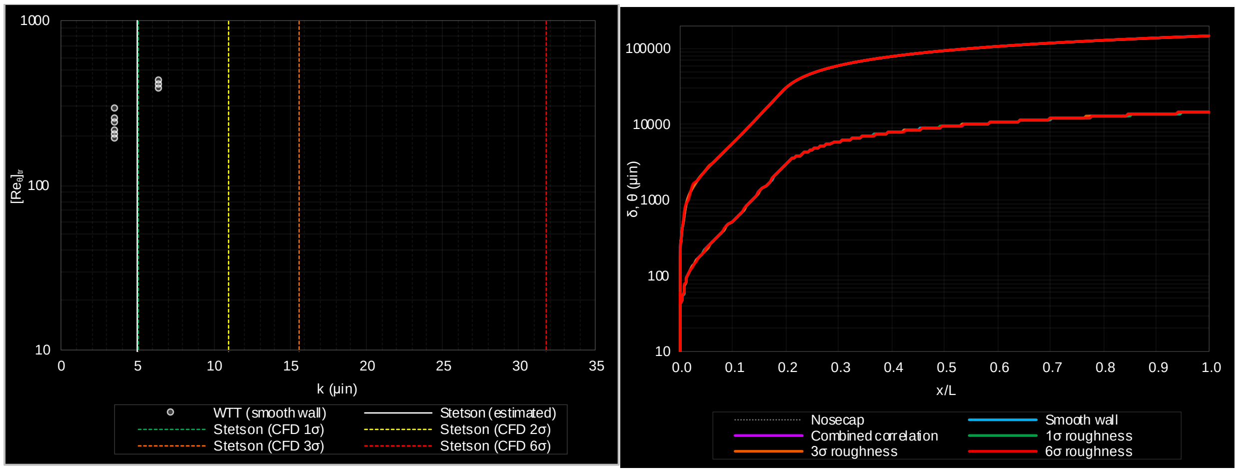

Fig. 13. Stetson modeled roughness compared with WTT roughness measurements (left) and comparison of δ (top) and θ (bottom) along x/L of increasing roughness for $k = 5\ \mu in$ (right).

Figure 14 (top left) shows $[Re_\theta]_{tr}$ as a function of k/δ for CFD simulations with increasing levels of stochastic roughness, shown alongside all experimental test data. The CFD roughness was set to $k = 5\ \mu in$ to represent a smooth-wall wind tunnel configuration and the baseline solution used the combined roughness-transition correlation. Notably, the CFD solutions did not align with the smooth-wall experimental data (flight tests and smooth-wall WTT), but did exhibit a similar slope when compared with the wind tunnel data. As roughness levels increased, the CFD solution trended closer to experimental data points.

The transition region was defined by $Re_\theta \sim 120$. The k/δ ratio was not used in this case due to the smooth wall assumption. Figure 14 (top right) shows $[Re_\theta]_{tr}$ as a function of $[X_{Combined}]$ and compares the Stetson CFD solutions with the PANT and combined correlations, and transition metrics are listed in Table 9.

Table 9. Predicted transition metrics (Stetson, $k = 5\ \mu in$).

Test Case	$[Re_\theta]_{tr}$	$[X_{correlation}]$	x/L	$[sta]_{tr}$
Stetson (smooth wall)	120	0.0005	0.0052	51
Stetson (1σ)	120	0.0010	0.0050	51
Stetson (3σ)	120	0.0080	0.0045	44
Stetson (6σ)	120	0.0165	0.0043	42

Figure 14 (bottom left) shows an upstream shift in transition locations as stochastic roughness levels increased. Figure 14 (bottom right) plots C_D as a function of R_q for different roughness levels, showing that drag increased with higher roughness, confirming the stochastic roughness model effectively captures roughness effects on the boundary layer. Drag predictions showed minimal discrepancy between the 1σ stochastic roughness case and Reda correlation solution, with a difference in C_D of only 0.0005%.

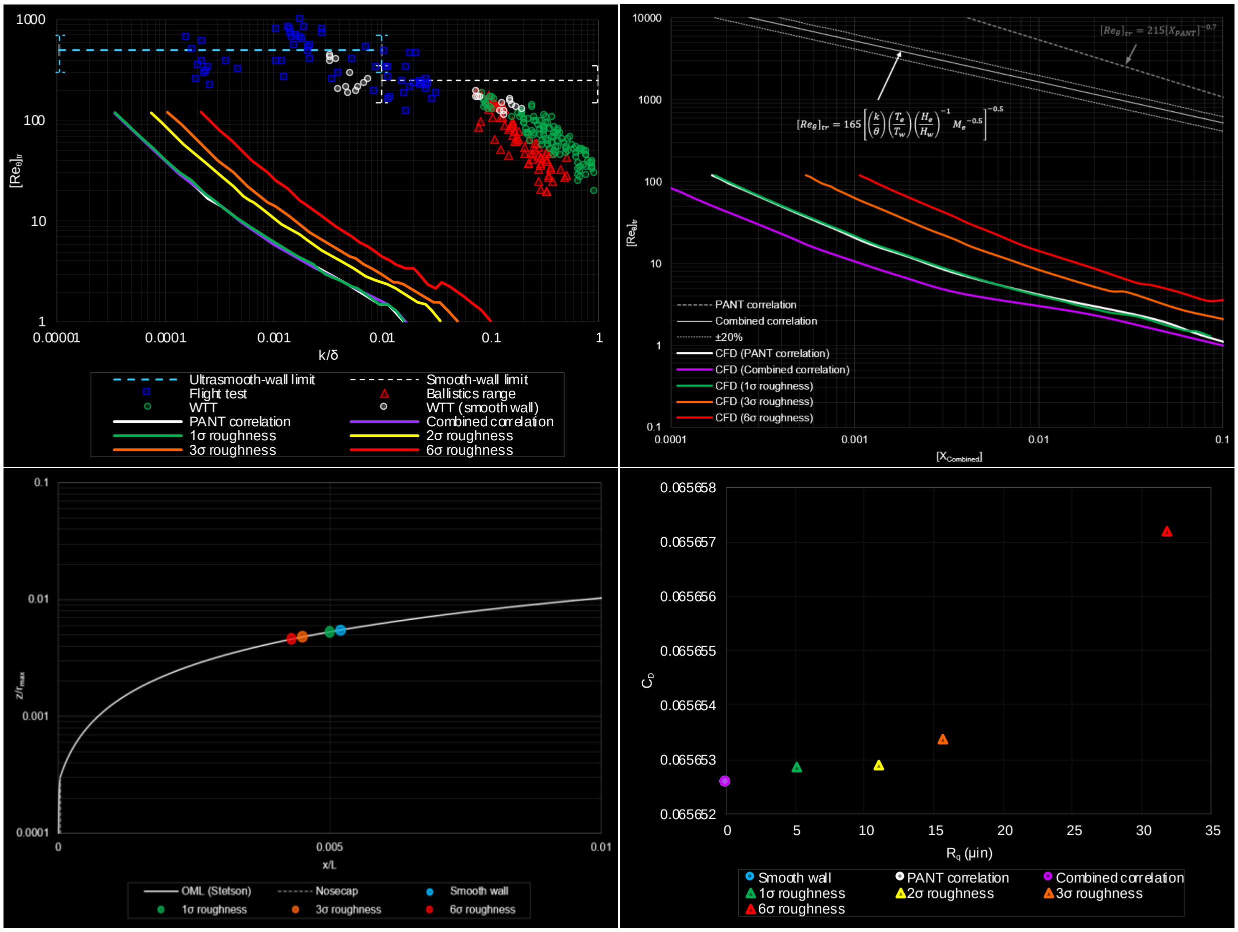

Fig. 14. Stetson transition analyses comparing $[Re_\theta]_{tr}$ versus k/δ and $[X_{PANT}]$ (top left and right) and effect of increasing roughness on transition location and C_D (bottom left and right).

C. Stability Analysis

The Langley Stability and Transition Analysis Code (LASTRAC) v2.1 was developed by NASA Langley and used to conduct stability analyses [14]. This code analyzes compressible boundary layer stability and predicts transition using contemporary linear stability theory or parabolized stability equation methods [4]. Although surface roughness was not the primary focus, the Stetson experiment produced notable hypersonic boundary layer stability data which correlated with theoretical instability predictions by Mack [16]. Because of its significance, LASTRAC analyses were conducted using the Stetson dataset to determine stochastic roughness effects on boundary layer stability.

Table 10 lists the Stetson test cases, predicted transition locations, and corresponding station numbers used as LASTRAC input values. Stability analysis was conducted across 100 stations, beginning at station 40 because this is just upstream of the earliest predicted transition location. A disturbance frequency range for second-mode instability was identified as 70.0–137.2 kHz, aligning closely with the second-mode frequency range of 70–150 kHz reported in [22] for the Stetson test.

Table 10. Range of stations analyzed and instability frequencies (Stetson).

Test Case	x/L	$[sta]_{tr}$	$[sta]_{range}$	ω (kHz)
Stetson (smooth)	0.0052	51	40-140	70.8-137.2
Stetson (combined correlation)	0.0052	51	40-140	70.5-136.9
Stetson (1σ)	0.0050	51	40-140	70.3-136.3
Stetson (3σ)	0.0045	44	40-140	70.0-136.0
Stetson (6σ)	0.0043	42	40-140	70.5-136.9

Figure 15 compares the N-factors across a range of frequencies, which shows the largest amplification occurring around 10 kHz for the solution using the combined roughness-transition correlation. Solutions from the higher stochastic roughness cases were inspected, which also showed peak amplification occurring around 10 kHz; this frequency was chosen to evaluate how the N-factor is affected as roughness levels increased. The 1σ roughness solution displayed a higher N-factor than the baseline solution generated with the combined correlation. However, the amplification factor decreased as roughness increased beyond 1σ. This was unexpected, but laminar mean flow solutions were used as inputs, so there was less confidence in the LASTRAC results. Additional stability analyses are recommended using more complex flow solutions to verify this observation.

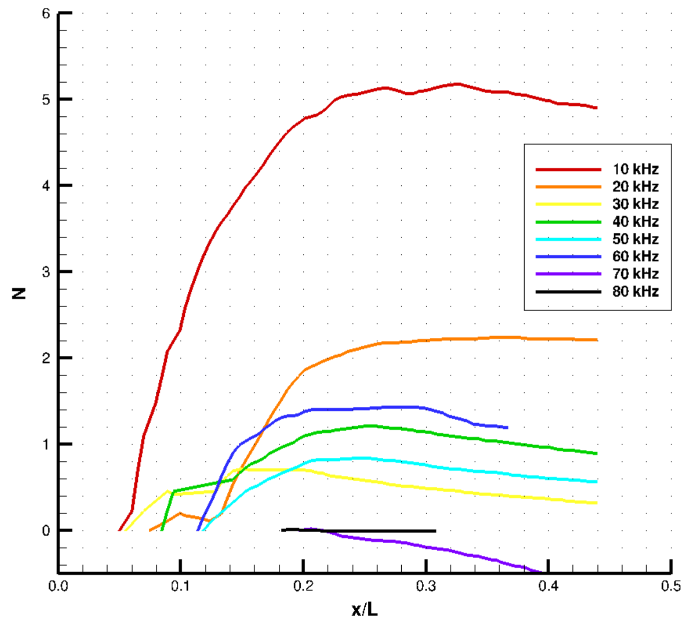

Fig. 15. N-factor as a function of axial length for the Stetson test case using the combined roughness-transition correlation ($k = 5\ \mu in$).

V. Summary and Future Research

A stochastic roughness model was implemented in the LAURA v5.6 CFD code and verified through a comprehensive assessment of OML geometries, roughness output statistics, and flow-field analyses. The model successfully generates stochastic roughness features that effectively represent realistic surface roughness characteristics. Output statistics confirm that the generated roughness is contained within user-defined bounds, further validating the model's accuracy and functionality. CFD results displayed good alignment with experimental test data when comparing $[Re]_{\theta_{tr}}$ to k/δ, a parameter traditionally used to differentiate smooth and rough-wall conditions. However, observations from PANT-J suggest that an upper roughness threshold likely exists, beyond which the k/δ parameter loses its effectiveness in defining smooth and rough-wall conditions. This is due to the rapid growth of δ at high roughness levels, which corrupts the reliability of this metric.

The PANT correlation showed good alignment with wind tunnel data. Stetson test cases displayed a similar trend despite having a different geometry, flow conditions, and surface roughness. This provides evidence that the disturbance parameter $[X_{PANT}]$ is effective in characterizing transition trends of wind tunnel data. However, some misalignment was observed with the Reda correlation when compared with ballistic range data. This discrepancy, also noted in the literature, suggests that $[X_{Reda}]$ may require re-evaluation for representing ballistic range transition trends.

Predicted transition locations were determined by calculating the disturbance parameter $[X_{correlation}]$, based on the transition parameter $[Re]_{\theta_{tr}}$. This disturbance parameter is mapped to an axial position, identifying the location where transition is predicted to occur. All cases showed that an increase in stochastic roughness levels corresponded to an upstream shift in the predicted transition location, indicating earlier transition onset. Additionally, CFD results showed that drag increased as roughness levels were increased. These trends confirm that increased roughness promotes earlier transition to turbulence, validating the stochastic roughness model's effectiveness in capturing roughness effects on hypersonic boundary layers.

The CFD stochastic roughness model demonstrated its capability to simulate realistic surface roughness effects on hypersonic boundary layers. By integrating roughness parameters as inputs, the model allows users to generate flow-field solutions which can be informed by actual surface roughness measurements. Solutions based on a statistical distribution captures the inherent randomness of realistic surface roughness and provides a capability to characterize the expected behavior in larger populations. The alignment between CFD results, experimental trends, and empirical correlations validates the model's effectiveness and utility as a tool for hypersonic transition prediction.

Continuation of this research could include integration of more ablation parameters, development of stochastic 3D roughness surfaces to model crossflow effects, additional model validation with DNS, and a comprehensive second-mode instability analysis on hypersonic cases. Reducing uncertainties in transition prediction can optimize design cycles and improve M&S accuracy for hypersonic systems. This research demonstrates that modeling stochastic roughness enhances hypersonic transition prediction capabilities and establishes a foundation for future improvements using this methodology.

VI. Acknowledgements

Special thanks to the U.S. Air Force STEM+M Program, AFLCMC/EBS, University of Florida Research & Engineering Education Facility for funding, support, and facility access to accomplish this research.

VII. References

[1] Alba, C., Johnson, H., Bartkowicz, M., Candler, G., & Berger, K. 2008 Boundary-Layer Stability Calculations for the HIFiRE-1 Vehicle. J. Spacecraft Rockets 45 (6).

[2] Bishop, W. 1976 Transition Induced by Distributed Roughness on Blunt Bodies in Supersonic Flow. Technical Report SAMSO-TR-76-146. Air Force Systems Command.

[3] Braslow, A. & Knox E. 1958 Simplified Method for Determination of Critical Height of Distributed Roughness Particles for Boundary-Layer Transition at Mach Numbers from 0 to 5. Technical Note 4363. National Advisory Committee for Aeronautics.

[4] Chang, C. 2004 Langley Stability and Transition Analysis Code (LASTRAC) Version 1.2 User Manual. Technical Manual TM-2004-213233. Langley Research Center, NASA.

[5] Chang, C., Malik, M. & Hussaini, M. 1990 Effects of shock on the stability of hypersonic boundary layers. AIAA Paper 90-1448.

[6] Clauser, F. 1954 Turbulent boundary layers in adverse pressure gradients, J. Aeronautical Sciences 21 (2).

[7] Colebrook, C. & White, C. 1937 Experiments with fluid friction in roughened pipes. Proceedings of the Royal Society of London 161 (906), 367-381.

[8] Dirling, R. 1977 On the relationship between material variability and surface roughness. AIAA Paper 77-402.

[9] Herbert, T. 1997 Parabolized stability equations. Annu. Rev. Fluid Mech. 29, 245-283.

[10] Hollis, B. 2019 Correlation of recent and historical hemispherical nose tip distributed roughness transition data. J. Spacecraft Rockets 56 (3).

[11] Hubs. 2021 What are the types of surface finishes for CNC machining? https://www.hubs.com/knowledge-base/surface-finishes-cnc-machinining/.

[12] Jackson, M. 1974 Passive Nosetip Technology (PANT) Program Volume XV. Roughness induced transition on blunt axisymmetric bodies – data report. Technical Report SAMSO-TR-74-86. Air Force Space and Missile Systems Organization.

[13] Kadviar, M., Tormey, D. & McGranaghan, G. 2021 A review on turbulent flow over rough surfaces: fundamentals and theories. Int. J. Thermofluids 10.

[14] LASTRAC, Langley Stability and Transition Analysis Code, Software Package, Ver. 1.2, Langley Research Center, Hampton, VA, 2011.

[15] LAURA, Langley Aerothermodynamic Upwind Relaxation Algorithm, Software Package, Ver. 5.6, Langley Research Center, Hampton, VA, 2020.

[16] Mack, L. 1984 Boundary-layer linear stability theory. AGARD Report No. 709, Part 3. Jet Propulsion Laboratory, NASA.

[17] Marineau, E. 2020 Chapter 2 – Compilation and analysis of second-mode amplitudes on sharp cones in hypersonic wind tunnels. In Hypersonic Boundary-Layer Transition Prediction, STO Technical Report TR-AVT-240. NATO.
[18] Marxen, O., Iaccarino, G. and Shaqfeh, S. 2014 Nonlinear instability of a supersonic boundary layer with two-dimensional roughness. J. Fluid Mech. 752, 497-520. DOI: 10.1017/jfm.2014.266.
[19] Reda, D. 1980 Correlation of nosetip boundary-layer transition data measured in ballistics-range experiments. AIAA J. 19 (3), 329-339.
[20] Reda, D. & Leverance, R. 1976 Boundary-layer transition experiments on pre-ablated graphite nosetips in a hyperballistics range. Technical Report NSWC/WOL/TR 76-71. White Oak Laboratory, Naval Surface Warfare Center.
[21] Schneider, S. 1999 Flight data for boundary-layer transition at hypersonic and supersonic speeds. J. Spacecraft Rockets 36 (1). DOI: 10.2514/2.3428.
[22] Stetson, K., Thompson, E. & Donaldson, J. 1983 Laminar boundary layer stability experiments on a cone at Mach 8, part 1: sharp cone. AIAA Paper 83-1761.
[23] Teague, E. 1982 Evaluation of Methods for Characterizing Surface Topography of Models for High Reynolds Number Wind Tunnels. AIAA Paper 82-0603.
[24] Thompson, K., Hollis, B., Johnston, C., Kleb, B., Lessard, V. & Mazaheri, A. 2020 LAURA User's Manual: 5.6. Technical Manual TM-2020-220566. Langley Research Center, NASA.
[25] Thompson, K., Johnston, C., Hollis, B. & Lessard, V. 2020 Recent improvements to the LAURA and HARA codes. AIAA Aviation 2020 Forum.
[26] van Driest, E. 1951 Turbulent boundary layer in compressible fluids. J. Aeronautical Sciences 18 (3).